The Septin Cytoskeleton is Required for Plasma Membrane Repair

M. Isabella Prislusky[1], Jonathan GT Lam[1], Viviana Ruiz Contreras [1,3], Marilynn Ng[1], Madeline Chamberlain[1], Madalyn Fields[1], Xiaoli Zhang[2], Amal O. Amer[1], Stephanie Seveau[1]

1-Department of Microbial Infection & Immunity, Wexner Medical Center, The Ohio State University, Columbus Ohio, USA.

2-Department of Biomedical Informatics, The Ohio State University, Columbus, Ohio, USA.

3-Grupo Investigaciones Biomédicas, Universidad de Sucre, Sincelejo, Sucre, Colombia.

Corresponding author: Stephanie Seveau, Seveau.1@osu.edu

Keywords: plasma membrane repair, septin, F-actin, annexin A2, cytoskeleton, *Listeria monocytogenes*, pore-forming toxin, listeriolysin O, cholesterol-dependent cytolysin.

ABSTRACT

Mammalian cells are frequently exposed to mechanical and biochemical stresses resulting in plasma membrane injuries. Repair mechanisms rapidly reseal the plasma membrane to restore homeostasis and prevent cell death. In the present work, a silencing RNA (siRNA) screen was performed to uncover the plasma membrane repair mechanisms of cells injured by the bacterial pore-forming toxin listeriolysin O (LLO). The screen identified a novel role for the septin cytoskeleton in mediating plasma membrane repair. Upon cell injury, the septin cytoskeleton partially dissociates from actin stress fibers and remodels with cortical F-actin and myosin-II to form loop (and ring)-like domains that protrude from the cell surface. These domains strictly colocalize with the calcium-dependent phospholipid-binding protein, annexin A2 (ANXA2). Importantly, formation of the SEPT/F-actin/ANXA2 domains are dependent on SEPT7 expression and is functionally correlated with the plasma membrane repair efficiency. Our studies open new research avenues by identifying a novel role for the septin cytoskeleton in remodeling the plasma membrane for its repair.

SUMMARY

Plasma membrane repair is a fundamental homeostatic process. Excessive damage or defective plasma membrane repair is associated with numerous pathological conditions. This work identifies a novel function of the septin cytoskeleton in remodeling the plasma membrane for its repair.

INTRODUCTION

The plasma membrane of mammalian cells forms a biophysical barrier that separates the cell from its external environment. Any mechanical or biochemical perturbations that compromise the integrity of the plasma membrane could be lethal for the cell. Therefore, mammalian cells have developed robust repair mechanisms which are critical for cellular and tissue homeostasis. Excessive plasma membrane damage or defective plasma membrane repair is involved in numerous pathological conditions including muscular dystrophies, ischemia-reperfusion, heart failure, chronic inflammation, and neurodegenerative diseases (Dias and Nylandsted, 2021). Furthermore, evolutionarily distinct pathogens including parasites, bacteria, and viruses perforate the host cell plasma membrane to exploit the host cell repair responses and successfully infect their host (Andrade, 2019; Ayyar et al., 2023; Banerji et al., 2021; Barisch et al., 2023; Bouillot et al., 2018; Thapa et al., 2020). In particular, the bacterial pathogen *Listeria monocytogenes* uses as a major virulence factor the pore-forming toxin listeriolysin O (LLO) that forms a pore complex across cholesterol-rich cytoplasmic and endosomal membranes (Osborne and Brumell, 2017; Petrisic et al., 2021). LLO-mediated plasma membrane perforation is moderate enough that effective plasma repair maintains cell viability to support the intracellular proliferation of the pathogen (Cassidy et al., 2012; Chen et al., 2018; Vadia and Seveau, 2014). However, transient cell perforation by LLO activates multiple signaling events that facilitate *L. monocytogenes* internalization, cell-to-cell spread, intracellular proliferation, and remodeling of the host cell transcriptome (Osborne and Brumell, 2017; Seveau, 2014; Vadia et al., 2011). How *L. monocytogenes*-infected cells repair their plasma membrane is not fully understood.

To uncover effectors that mediate the repair of LLO-perforated cells, we performed a siRNA screen targeting 245 protein-coding genes controlling endocytosis, exocytosis, and intracellular trafficking. The screen identified 57 candidates including previously known plasma membrane repair proteins such as calpain 1, the acid sphingomyelinase (ASM), several annexins, and the endosomal sorting complexes required for transport (ESCRT)-III. Our screen also identified novel plasma membrane repair candidates. Of those, we focused on septin 7 because the septins are an important family of highly conserved eukaryotic proteins described as the fourth component of the cytoskeleton after F-actin, microtubules, and intermediate filaments. The septins play central roles in major cellular functions such as cytokinesis and cell migration by forming filaments and rings that control the shape and properties of the plasma membrane (Benoit et al., 2023). However, the septin cytoskeleton has not been previously shown to repair the plasma membrane. Septin 7 plays a critical role in the formation of septin filaments as it is the only non-redundant septin among the 13 human septin family members (Abbey et al., 2016;

Kinoshita, 2003). Furthermore, little is known about the role of the cytoskeleton in repairing cells injured by pore-forming toxins. Using various complementary approaches, our data support a novel role for the septin cytoskeleton in mediating plasma membrane repair by controlling the formation of membrane domains containing annexin A2 and the cortical actomyosin cytoskeleton.

RESULTS

A siRNA screen identifies candidate genes controlling plasma membrane repair of LLO-perforated HeLa cells

To reveal the components involved in the plasma membrane repair mechanisms of LLO-perforated HeLa cells, we screened a library of siRNAs that target 245 human genes controlling endocytosis, exocytosis, intracellular trafficking, and the cytoskeleton (Supplemental Table 1). Each gene was targeted for 72 h by a cocktail of three siRNAs with non-overlapping sequences. To assess the plasma membrane repair efficiency of siRNA-treated cells, we used a fluorescence-based assay that measures plasma membrane integrity and enumerates cells in a temperature-controlled plate reader equipped for dual spectrofluorometric and fluorescence microscopy measurements (Lam et al., 2019). In this assay, HeLa cells expressing green-fluorescent histone 2B (H2B-GFP) were exposed, or not, to sub-lytic LLO concentrations for 30 min at 37°C in the presence of the membrane-impermeant dye TO-PRO-3. TO-PRO-3 exhibits a marked increase in fluorescence intensity upon binding to nucleic acids. The influx of TO-PRO-3 into cells was quantified via spectrofluorometric measurement and served as a read-out for plasma membrane integrity. The total number of cells in each well was enumerated based on their nuclear fluorescence (H2B-GFP), pre- and post-kinetic.

We found that the silencing of 217 proteins resulted in cell numbers ranging from 85-115% relative to control cells. Gene knockdown (KD) resulting in cell densities outside of this range were excluded (10 gene KD with cell counts >115% and 18 with cell counts <85% of control cells were excluded) (Supplemental Table 2). Importantly, cells did not detach during the assay as the average cell count ratio, defined as the cell count post-kinetic relative to the cell count pre-kinetic, was unaffected in all samples, and across all siRNA- and LLO-treatment conditions was 1.0061 ± 0.0065 (average ± SEM). We identified 57 genes which silencing affected membrane integrity, either positively (47) or negatively (10) (Supplemental Table 3). These include genes encoding proteins previously shown to control plasma membrane repair such as the annexins (ANXA2, ANXA7, and ANXA11), the lysosomal enzyme acid sphingomyelinase (SMPD1), calpain 1 (CPN1), and the ESCRT-III machinery (CHMP2) (Jimenez et al., 2014; Mellgren et al., 2007; Satoh et al., 2002; Sonder et al., 2019; Tam et al., 2010). The screen further identified genes involved in membrane fusion (4 synaptotagmins and 12 SNAREs), lysosome biogenesis and functions (HPS3, HPS5, M6PRBP1, AP3S2, AP3M2, AP3S1, and Rab7) and genes involved in exocytosis and the secretion of exosomes (EXOC1, EXOC6, Rab27A, Rab27B, and Rab11A)(Escrevente et al., 2021). Conversely, four genes encoding endocytic molecules had a

negative effect (DNM2, CTLA, CTLB, AP2S1). Several genes controlling the actin cytoskeleton were positive hits (IQSEC1, ABI1, GBF1, and SEPT7). Of these candidates, we focused on SEPT7 because septins are a major family of cytoskeletal proteins that had not previously been shown to control plasma membrane repair.

The septins are required for plasma membrane repair of LLO-perforated cells

To confirm the role of the septins in plasma membrane repair, we first measured the knockdown efficiencies of each siRNA used in the primary screen targeting SEPT2, SEPT6, SEPT7, and SEPT9 (Figure 1A and Supplemental Figure (SF) 1A-1D). We found that SEPT7, SEPT9, and SEPT2 protein levels were decreased by 90-95% compared to control cells that were treated with the non-targeting siRNA. However, SEPT6 expression was only decreased by about 35-40% for two of the three siRNA tested. Also, as previously reported by others, decreasing SEPT7 expression reduced SEPT2, SEPT6, and SEPT9 protein levels, whereas targeting SEPT2, SEPT6, and SEPT9 did not appear to significantly affect the expression of the other tested septins (SF 1A-1D) (Kremer et al., 2005). We then evaluated the effect of silencing septin expression on the plasma membrane integrity of LLO-perforated cells. Silencing SEPT7 with each siRNA resulted in a significant loss in plasma membrane integrity of LLO-treated cells (Figure 1B). This was unlikely due to an off-target effect of the siRNAs because three non-overlapping siRNA sequences were tested independently. To distinguish if the loss in plasma membrane integrity of SEPT7-deficient cells was due to an increase in plasma membrane susceptibility to LLO perforation or to a defect in plasma membrane repair, we measured the integrity of cells exposed to LLO in Ca^{2+}-free medium, an experimental condition preventing plasma membrane repair. We found that in Ca^{2+}-free medium, plasma membrane damage was similar in control and SEPT7-deficient cells leading to the conclusion that plasma membrane repair is defective in SEPT7-deficient cells (Figure 1C). Although the primary screen did not reveal a role for SEPT6, we found that SEPT6-siRNA1 and SEPT6-siRNA3, which each reduces SEPT6 expression, markedly affected plasma membrane repair (Figure 1C, D). As observed in the primary screen, knocking down the expression of SEPT2 and SEPT9 did not affect plasma membrane integrity (Figure 1C, E, F).

To further establish the role of SEPT7 in plasma membrane repair, we generated two stable HeLa cell lines with doxycycline-inducible expression of short hairpin RNA (shRNA) targeting SEPT7. Two SEPT7 non-overlaping silencing sequences, distinct from the three siRNA sequences used in the screen, were tested (D_iSEPT7-shRNA1 and D_iSEPT7-shRNA2 HeLa cells) (Figure 1G and SF 1E). We selected the D_iSEPT7-shRNA1 cell line for its lowest expression of

SEPT7 protein in the presence of doxycycline, and we repeated the repair assay comparing the repair ratio of doxycycline-treated to non-treated in D_iSEPT7-shRNA1 and control HeLa cells (Figure 1H). In Ca^{2+}-free medium, doxycycline treatment alone increased HeLa cell damage independently of SEPT7 expression but had no direct effect on LLO pore formation as measured via a hemolytic assay (red blood cells do not repair LLO pores) (SF 1F). Therefore, doxycycline increases the cell intrinsic susceptibility to perforation by LLO. Most importantly, plasma membrane repair of SEPT7-deficient cells was significantly impaired in comparison to control cells, which confirmed the role of SEPT7 in plasma membrane repair of LLO-injured cells (Figure 1H).

As a complementary approach to establish if the septin cytoskeleton plays a role in plasma membrane repair, we used the pharmacological agent forchlorfenuron (FCF), which is known to reversibly bind to and stabilize septin oligomers and/or filaments (DeMay et al., 2010; Hu et al., 2008; Iwase et al., 2004). Cell treatment with FCF resulted in a significant decrease in plasma membrane damage of LLO-treated cells (Figure 1I, SF 1G, H). We determined if this was due to enhanced plasma membrane repair, a decreased susceptibility of the cells to perforation by LLO, or a direct inhibitory effect of FCF on LLO pore formation. In Ca^{2+}-free medium, FCF treatment did not affect cell susceptibility to LLO-perforation (Figures 1I, SF 1G, 1H) and FCF didn't affect LLO pore formation as shown by a hemolytic assay despite the presence of a large concentration range of FCF (SF 1I). These data support that FCF increases plasma membrane repair efficiency of LLO-treated cells. Collectively, our data strongly support a novel role for the septin cytoskeleton in plasma membrane repair of cells perforated by LLO. Of note, the strongest inhibition of plasma membrane repair was observed in SEPT7-deficient cells, which is most likely due to the essential and non-redundant activity of SEPT7, whereas SEPT2, SEPT6, and SEPT9 are functionally redundant (Spiliotis and Nakos, 2021). In addition, knocking down SEPT7 imparts pleiotropic effects on the expression of multiple other septins as we and others observed (Kremer et al., 2005).

The septin cytoskeleton is remodeled to form loop and ring structures that colocalize with F-actin, myosin-IIA, and annexin A2 in LLO-injured cells

To analyze the role of the septins in plasma membrane repair, HeLa cells were treated, or not, with LLO for 5 to 15 min followed by chemical fixation and fluorescent labeling of SEPT2, SEPT7, and SEPT9. Due to its low expression level, SEPT6 labeling was very faint and was not carried out. The septin cytoskeleton is known to regulate and colocalize with the actin cytoskeleton (Benoit et al., 2023). Therefore, we studied the subcellular distribution of the septins

relative to F-actin. We found that SEPT2, SEPT7, and SEPT9 display similar labeling patterns in all experimental conditions. This was expected since septin hexamers (SEPT-2,-6,-7,-7,-6,-2) and octamers (SEPT-2,-6,-7,-9,-9,-7,-6,-2) co-assemble to form filaments or rings (Benoit et al., 2023). Septin filaments mostly colocalized with the actin stress fibers in control untreated HeLa cells (Figure 2A, SF 2A). Strikingly, in LLO-treated cells, a large fraction of the septin cytoskeleton dissociated from the actin stress fibers in LLO-treated cells (Figure 2, SF 2A, D) and reorganized together with F-actin leading to the formation of knob- and loop (or ring)-like structures (Figure 2, SF 2A), which formation increased over time from 5 to 15 min post-LLO-exposure (Figure 3, SF 2B). Septins are known to control the assembly of contractile F-actin rings during cytokinesis, therefore, we labeled cells with and anti-myosin-IIA antibodies to establish if the newly formed F-actin ring structures could also be contractile. As shown in Figure 4A, the knob- and loop-like structures of septin/F-actin cytoskeleton colocalized with myosin-IIA. The septins may control the organization of membrane domains specialized in plasma membrane repair. Therefore, we investigated if the remodeled septins codistribute with annexin A2 (ANXA2) and ALG-2-interacting protein X (ALIX), which are known to control plasma membrane regions undergoing repair (Koerdt et al., 2019; Sonder et al., 2019). ALIX formed larger puncta in LLO-treated cells in comparison to control cells but rarely colocalizes with the septins (SF 2C). However, in the presence of LLO, there was a clear colocalization of the septins and ANXA2, as observed in cells transiently expressing ANXA2-GFP and in cells fluorescently labeled with anti-ANXA2 antibodies (Figure 4B, 4B'). We found that the septins display almost 100% colocalization with both F-actin and ANXA2, including within the knob/loop structures (Figure 4B, 4B' 4C). This codistribution of ANXA2, the septins, and F-actin was observed throughout the cell and within the knob and loop structures. In conclusion, the septin cytoskeleton, visualized via labeling of SEPT2, SEPT7, or SEPT9, is remodeled in LLO-treated cells to colocalize with ANXA2 and F-actin/myosin cytoskeleton. These domains further rearrange to form curved structures that we described as knobs and loops.

Redistribution of the septin cytoskeleton is functionally correlated with plasma membrane repair efficiency and occurs at the plasma membrane

If the septin cytoskeleton is remodeled to repair the plasma membrane, such remodeling should be functionally correlated with the plasma membrane repair efficiency. Thus, septin remodeling should not occur (or its occurrence should decrease) when plasma membrane repair is prevented (in Ca^{2+}-free medium) and its remodeling should increase when plasma membrane repair is enhanced (in the presence of FCF). Consistent with this scenario, formation of the septin/F-actin knobs and loops and ANXA2 redistribution were markedly decreased when cells

were exposed to LLO in Ca^{2+}-free medium (Figure 5A). The number of knobs and loops per cell and the percentage of cells presenting such structures, were significantly decreased in LLO-treated cells in Ca^{2+}-free medium compared to Ca^{2+}-replete medium (Figure 5B, C). Also consistent with this scenario, FCF treatment led to a significant increase in the number of septin knobs and loops per cell, which all colocalized with F-actin and ANXA2 (Figure 5B, C, D).

If the septin cytoskeleton is remodeled to form domains that repair the plasma membrane, these domains should localize proximal to the plasma membrane. To better establish the subcellular localization of the remodeled septin cytoskeleton, HeLa cells were transiently transfected to express the fluorescent plasma membrane marker Lck-mTurquoise2 (Zacharias et al., 2002). As shown in Figure 6A, SEPT2 and F-actin colocalized with LcK-mTurquoise2. We next performed three-dimensional analyses to localize the remodeled septin cytoskeleton relative to the cell surface. These analyses showed that the septin/F-actin/ANXA2 knob and loop structures are present on the cell surface and often protrude outward of the cell surface (Figure 6B to D). Together, these data show that in response to LLO-mediated plasma membrane perforation, the septin cytoskeleton is remodeled together with ANXA2 and F-actin into submembranous loop and ring-like structures in a calcium-dependent fashion and this remodeling is correlated with the plasma membrane repair efficiency.

The septins control the remodeling of F-actin and ANXA2 during plasma membrane repair

The septins are known to regulate F-actin dynamics during cytokinesis (Russo and Krauss, 2021) and ANXA2 is known to control plasma membrane repair of cells mechanically damaged and perforated by pore-forming toxins (Jaiswal et al., 2014; Ray et al., 2022). To establish if the septin cytoskeleton is upstream or downstream from ANXA2 recruitment and F-actin knob and loop formation, we next, knocked down SEPT7 expression and labeled cells for F-actin and ANXA2. In SEPT7-deficient cells, labeling of the septin cytoskeleton with anti-SEPT2, 7, or 9 Abs was markedly decreased in accordance with the essential role of SEPT7 in the expression of several septin members and in the formation of septin filaments (Figure 7A, SF 2D). The formation of F-actin knobs and loops was markedly decreased in SEPT7-deficient cells, which indicates that the septins are essential for the remodeling of cortical F-actin (Figure 7A, B). Importantly, the few F-actin loops observed in SEPT7-deficient cells colocalized with low levels of septins. Furthermore, in SEPT7-deficient cells, ANXA2 labeling was unaffected in the absence of LLO. However, there was a substantial decrease in ANXA2 recruitment in SEPT7-deficient cells exposed to LLO in comparison to SEPT7-proficient control cells. Collectively, our data

support that the septin cytoskeleton is required for the formation and/or stabilization of plasma membrane repair domains that contain ANXA2 and actomyosin.

DISCUSSION

This work identified a novel role for the septin cytoskeleton in plasma membrane repair. The model pore-forming toxin, listeriolysin O (LLO), which belongs to the cholesterol-dependent cytolysins (CDC) /Membrane Attack Complex/Perforin (MACPF) superfamily was used to inflict plasma membrane damage (Dunstone and Tweten, 2012). We report that septin-deficient cells (SEPT7 and SEPT6) display impaired plasma membrane repair, whereas cells treated with the septin cytoskeleton stabilizing agent FCF display enhanced plasma membrane repair. During plasma membrane repair, the septin cytoskeleton partially dissociates from actin stress fibers and forms subplasmalemmal domains with F-actin and myosin-IIA which further rearrange to form loops and rings that often protrude from the cell surface. This remodeling is SEPT7- and Ca^{2+}-dependent and is correlated with the plasma membrane repair efficiency (Figures 5A-5C, Figure 7A, 7B). Collectively, these data strongly support the role of the septins in remodeling the plasma membrane of LLO-injured cells for its repair. This conclusion is further supported by the fact that SEPT7 is required for ANXA2 recruitment and ANXA2 colocalize with redistributed septin/actin cytoskeletons in LLO-injured cells. ANXA2 is a Ca^{2+}-dependent protein critical for plasma membrane repair in CDC-injured cells and that was also identified in our screen (Supplemental Table 3)(Koerdt et al., 2019; Ray et al., 2022). Therefore, the septin cytoskeleton appears to be important for the formation and/or stabilization of membrane domains specialized in plasma membrane repair.

Several calcium-dependent mechanisms have been shown to repair the plasma membrane of cells mechanically damaged or perforated by pore-forming toxins. The fusion of intracellular vesicles/organelles followed by their exocytosis at the wound site (Bi et al., 1995; Rall, 2019) decrease the surface tension and patch the membrane wounds (McNeil, 2002; Togo et al., 2000). More recently, it was shown that caveolae-dependent endocytosis and/or membrane shedding remove damaged portions of the plasma membrane (Idone et al., 2008; Jimenez et al., 2014; Ray et al., 2022). In another model, F-actin-driven constriction either closes the membrane wounds or promotes the excision of the edges of the ruptured plasma membrane in mechanically wounded cells (Bement et al., 1999; Jaiswal et al., 2014). However, little is known about the role of the cytoskeleton in the repair of cells injured by pore-forming toxins. Our screen indicates that membrane fusion, lysosome exocytosis, annexins- and ESCRT-III are important to repair LLO-injured cells. Therefore, it is likely that several repair mechanisms act together to reseal the LLO-injured cells.

Identification of SEPT7 as a potential repair protein was novel. The septins are an important family of eukaryotic proteins described as the “fourth element of the cytoskeleton” after

actin filaments, microtubules, and intermediate filaments (Benoit et al., 2023; Robertin and Mostowy, 2020; Spiliotis and Nakos, 2021). Septins are GTP-binding proteins divided into four groups based on sequence homology (SEPT 2, 3, 6, and 7), each of which includes several redundant members except for SEPT7, the only member of its group. Septin members of each group assemble into hetero-hexameric or hetero-octameric complexes which further organize into filaments. They bind to membranes to form diffusion barriers, and act as scaffolding proteins that interact with multiple cellular components including inositol phosphates, SNARE machinery, clathrin, actin, motor proteins, and tubulin. Through these interactions, the septins control multiple processes that encompass signaling, membrane fusion, membrane curvature, endocytosis, and exocytosis. Therefore, the septins might be multifunctional during plasma membrane repair as several of the cellular machineries they regulate are also important for plasma membrane repair. The present studies highlight a role for the septins in the remodeling of the plasma membrane into domains that include F-actin, myosin IIA, and ANXA2. The septins are known to bind actin filaments altering their curvature, which is in accordance with the observed septin/F-actin loops and rings formed during plasma membrane repair (Benoit et al., 2023). The increased formation of septin loops in FCF-treated cells improved membrane repair, consistent with a role for these structures in plasma membrane repair. This latter results were a surprise as FCF was proposed to disrupt septin functions (Iwase et al., 2004). However, mechanisms by which FCF alters the septin dynamics are still not completely understood and need further elucidation. In particular, FCF has been shown to facilitate septin assemblies (DeMay et al., 2010; Hu et al., 2008). Similarly, our data show that FCF significantly increased septin loop formation in LLO-treated cells.

The plasmalemmal domains that include ANXA2 and septin/F-actin/myosin-II form loop structures which size ranges from 2 to 6 μm in diameter and protrude from the cell surface. Functionally, these structures could act as membrane domains for the sequestration, inactivation, and/or removal of LLO pores. The septins are known to organize and bend the acto-myosin cytoskeleton during cytokinesis (Mavrakis et al., 2014; Nakamura et al., 2023) and ANXA2 is required for cytokinesis (Benaud et al., 2015). Therefore, septin-dependent reorganization of the cortical F-actin network during cytokinesis and plasma membrane repair likely share common mechanisms. Previous studies showed that ANXA2 and the protein S100A11 control cortical F-actin to repair mechanically ruptured cells by excision (Jaiswal et al., 2014). Furthermore, ANXA2 was shown to control plasma membrane shedding of cells injured by the pore-forming toxin streptolysin O (Ray et al., 2022). Therefore, the septins likely control the organization of plasma membrane domains to sequester LLO and/or to shed the membrane associated with LLO pores.

Based on the presence of ANXA2, these membrane domains likely specialize in shedding damaged portions of the plasma membrane (Jaiswal et al., 2014; Ray et al., 2022). Based on their actomyosin enrichment, these domains may control the localization and segregation of damaged portions of the membrane. Our screen also identified CHMP2 and ANXA7 (Supplemental Table 3) which supports that the ESCRT-III machinery also repairs LLO-injured cells by shedding (Jimenez et al., 2014; Sonder et al., 2019). However, ALIX, a protein that recruits the ESCRT-III machinery at plasma membrane wounds, did not colocalize with the septin/F-actin loops. These findings suggest that plasma membrane repair involves several mechanisms which together maintain cell integrity. Whether these mechanisms coexist or operate in different time scales will need to be established.

L. monocytogenes is a facultative intracellular pathogen, which intracellular replication is essential for pathogenesis. Paradoxically, this bacterium uses the pore-forming toxin LLO as its major virulence factor, yet infected cells remain viable to support bacterial replication. Viability of infected cells results from LLO intrinsic properties that reduces its activity (Chen et al., 2018; Rogers et al., 1986; Schuerch et al., 2005; Seveau, 2014). The pores formed by LLO perforate cholesterol-rich cytoplasmic and endocytic membranes during *L. monocytogenes* phagocytosis and cell-to-cell spreading of the pathogen (Czuczman et al., 2014; Goldfine et al., 1995; Goldfine et al., 2000; Vadia et al., 2011). We and others have shown that *L. monocytogenes*-infected cells undergo plasma membrane repair in the first 30 min of infection and when bacteria replicate in the host cell cytosol (Cassidy et al., 2012; Vadia and Seveau, 2014). Therefore, viability of infected cells results from the combination of LLO intrinsic properties with the plasma membrane repair processes. The septins were previously shown to regulate *L. monocytogenes* internalization and to form a cage-like structure around cytosolic bacteria (Robertin and Mostowy, 2020). Our data highlight a novel function of the septins in the repair of host cells perforated by LLO. It will be important to establish if the roles of the septins in bacterial uptake and in their cytosolic entrapment are influenced by LLO-induced host cell perforation.

During the inflammatory and immune responses, several host pore-forming proteins that belong to the MAC/PF superfamily and the gasdermin family, perforate host cells and elicit plasma membrane repair (Nozaki et al., 2022). Similar to LLO-perforated cells, plasma membrane repair of cells damaged by endogenous pore-forming proteins may involve the septin cytoskeleton. In conclusion, our studies open new research avenues on the role of the septin cytoskeleton in maintaining plasma membrane integrity relevant to the many physiological and pathological conditions involving plasma membrane repair.

MATERIALS and METHODS

Cell culture and reagents. HeLa cells have been extensively used to identify plasma membrane repair mechanisms and are highly amenable to transfection with siRNAs. HeLa cells (ATCC, # CCL-2™) and HeLa Histone 2B-GFP (HeLa H2B-GFP, EMD Millipore SCC117) were cultured in Dulbecco's Modified Eagles Medium (DMEM, Gibco #11995) containing 10% heat-inactivated fetal bovine serum (HIFBS), 100 units/ml penicillin and 100 µg/ml streptomycin at 37°C and 5% CO_2 atmosphere. Repair permissive buffer (M1) (Hanks Balanced Salt Solution (HBSS, Gibco #14175) supplemented with 0.5 mM $MgCl_2$, 1.26 mM $CaCl_2$, 25 mM glucose, and 10 mM HEPES) and repair restrictive buffer (M2) (HBSS supplemented with 0.5 mM $MgCl_2$, 25 mM glucose and 10 mM HEPES) buffers were used for the repair assays. For lentiviral production, Lenti-X™ 293T Cell Line (Takara) was cultured in 90% DMEM with high glucose (4.5 g/L), 4 mM L-glutamine, and 10% FBS; 100 units/ml penicillin G sodium, and 100 µg/ml streptomycin sulfate. When appropriate, the cell culture medium contained the Tet-system-approved FBS (Takara). Recombinant six-histidine-tagged LLO was purified from *E. coli* as previously described (Vadia et al., 2011). The hemolytic activity of LLO was measured as previously described (Vadia et al., 2011). In all of our experimental conditions, cells are viable and fully recover from LLO injury (Lam et al., 2018; Vadia et al., 2011; Vadia and Seveau, 2014). The stock solution of Forchlorfenuron (Sigma, 32974) was prepared in DMSO at 50 mM. Anti-SEPT2 (Protein Tech, mouse clone 2F3B2, for Western Blot; Atlas, Rabbit polyclonal for imaging), anti-SEPT6 (Protein Tech rabbit polyclonal for Western Blot and imaging), anti-SEPT7 (Protein Tech rabbit polyclonal for Western Blot and imaging), anti-SEPT9 (Atlas, rabbit polyclonal for Western Blot and imaging), anti-annexin A2 (Invitrogen, mouse clone Z014), anti-Alix (Biolegend, clone 3A9), anti-myosin-IIA (Abnova, clone 2B3), anti-tubulin (Sigma, clone B-5-1-2), Alexa Fluor 488 conjugated Phalloidin (Invitrogen, #A12379) and Alexa Fluor 647 conjugated Phalloidin (Invitrogen, #A22287) were the primary antibodies used for immunoblotting and fluorescence microscopy experiments. The secondary antibodies used were anti-mouse IgG horseradish peroxidase (HRP)-conjugated (Cell Signal Technology, #7076S), anti-rabbit IgG (HRP)-conjugated (Cell Signal Technology, #7074S), anti-mouse IgG Alexa Fluor-conjugated (Invitrogen), anti-rabbit IgG Alexa Fluor-conjugated (Invitrogen). The vector Lck-mTurquoise2, in the backbone pEGFP-C1, was a gift from Dorus Gadella (Addgene #98822) (doi: https://doi.org/10.1101/160374). The vector encoding annexin A2-GFP, in the backbone pEGFP-N3, was a gift from Volker Gerke & Ursula Rescher (Addgene # 107196) (Rescher et al., 2000). EZ-Tet-pLKO-Puro (Addgene #85966) was a gift from Cindy Miranti and both psPaX2 (Addgene #12260), and pMD2.G (Addgene #12259)

were gifts from Didier Trono (Frank et al.). Cells were transiently transfected using Lipofectamine 2000 (Invitrogen) and Opti MEM according to the manufacturer's instruction.

Generation of inducible SEPTIN7 shRNA HeLa cell lines. To generate doxycycline-inducible SEPT7 shRNA stable HeLa cell lines, annealed oligonucleotides encoding shRNA sequences were cloned into the lentiviral vector EZ-Tet-pLKO-Puro using the restriction sites NheI and EcoRI (Frank et al., 2017). The resulting constructs were validated by sequencing. The sequences of the oligonucleotides and primers are presented in Supplemental Table 4. For lentiviral production, Lenti-X™ 293T cells were transfected with the vectors pMD2.G, psPAX2, and EZ-Tet-pLKO-Puro using Lipofectamine 2000 and Opti MEM according to the manufacturer's instructions (Invitrogen). Lentiviruses were collected after precipitation using PEG-IT (System Biosciences). HeLa cells were transduced using serial dilutions of lentiviral suspension and were cultured with 1 µg/ml puromycin. Wells corresponding to viral titers leading to the growth of small, isolated colonies were pooled and further cultured. Stable HeLa- D_iSEPT7-shRNA1 and D_iSEPT7-shRNA2 were cultured with 50 ng/ml doxycycline (DOX) for 72 h and SEPT7 expression was measured by immunoblotting (Figure 2G, SF 1E).

Septin Immunoblotting. HeLa cells were lysed (150 mM NaCl, 20 mM Tris HCl, 2 mM EDTA, NP40 1% and protease inhibitors (Roche # 04693132001, pH 7.4), and cell lysates were boiled in reducing Laemmli buffer. BCA (BioRad) protein assay was carried out to adjust the volumes of loaded samples. Lysates were subjected to SDS-PAGE electrophoresis and transferred to PVDF membranes. Membranes were labeled with the indicated septin antibodies and then stripped (2.35 % SDS, 73.5 mM Tris HCl pH 6.8, 134.6 mM beta-mercaptoethanol) and labeled with tubulin as a loading control. The knockdown efficiencies were measured using Image Lab (BioRad).

siRNA screen. To identify novel genes controlling plasma membrane repair, a siRNA screen was performed in 96-well tissue culture-treated clear bottom black plate (Corning). HeLa H2B-GFP were plated at $7x10^3$ cells/well (DMEM, 10% HIFBS) and reverse transfected with 1 pmol/well of a combination of 3 non-overlapping 11-mer siRNAs (Ambion Silencer® Select, Thermofisher) using Lipofectamine RNAiMax transfection reagent (Invitrogen) and Opti-MEM Reduced Serum Medium (Gibco) according to the manufacturer's instructions. For the list of targeted genes and siRNA sequences, see Supplemental Table 1. To account for potential variations in cell growth during the 72-hour treatment with the various siRNAs, control cells were plated at three different concentrations and treated with a non-targeting siRNA. Three sets of control cells were prepared

in each plate by reverse transfection of $7x10^3$, $6.3 x10^3$, and $5.6 x10^3$ cells/well with 1 pmol of non-targeting Silencer Select negative control siRNA No. 1 (Invitrogen). All experimental conditions were carried out in quadruplicates. The cells were incubated at 37°C and 5% CO_2 atmosphere for 72 hours. To assess membrane resealing in the presence or absence of Ca^{2+}, the top half of the siRNA-treated cells plate (plate 1) was washed twice with 37°C 200 µl of buffer M1 and replaced with 100 µl of M1 containing 1 µM TO-PRO-3 iodide (ThermoFisher). The bottom half of the plate was washed once with 37°C 200 µl of buffer M2 containing 5 mM ethylene glycol-bis(2-aminoethylether)-N, N, N', N', tetraacetic acid (EGTA), followed by a wash with 200 µl of buffer M2, and replaced with 100 µl of buffer M2 containing 1 µM TO-PRO-3 iodide (ThermoFisher). A SpectraMax i3X multimode detection platform equipped with a MiniMax cytometer (Molecular Devices) was used to obtain fluorescent kinetic readings and 4X magnification images (transmitted light, and green and red fluorescence; 535 nm and 638 nm excitations and 617 nm 665 nm emissions respectively). Pre-kinetic images were acquired as previously described (Lam et al., 2019). The 96-well cell culture plate was cooled to 4°C for 5 min and ice-cold LLO and TO-PRO-3 iodide were added in M1 or M2 at 0.5 nM and 1 uM final concentrations, respectively. The plates were then placed into the spectrofluorometer for the 30 min kinetic assay at 37°C, then post-kinetic fluorescence images were acquired as described previously (Lam et al., 2019). For analysis, cells were enumerated in each well, as previously described (Lam et al., 2019). Experimental conditions in which siRNA-treated wells exhibited cell densities greater than or less than 15% compared to control wells were not considered (Supplemental Table 2). Control wells with the closest cell count to the specific knockdown condition were chosen for comparison. The average TO-PRO-3 fluorescence intensities at time point 30 min were log-transformed and then analyzed with ANOVA to establish the list of candidate genes with positive or negative effects, respectively, in plasma membrane repair.

Plasma membrane repair assays. All plasma membrane repair assays (cells treated with siRNAs, shRNAs, or pharmacological agents) were based on measuring the intracellular incorporation of TO-PRO-3, as detailed above in the siRNA screen. Cells were plated in 96- or 24-well plates and treated with siRNA and/or drugs (doxycycline, DMSO, or FCF) for the indicated times prior to the assay. Cells were washed two times with 37°C M1 buffer and supplemented with M1 containing 1.5 µM TO-PRO-3 iodide. For calcium-free conditions, cells were washed once with 37°C buffer M2 containing 5 mM EGTA, followed by a wash with buffer M2, and buffer M2 containing 1 µM TO-PRO-3 iodide. Cells were then incubated in the presence or the absence of 0.5 nM LLO. In some experiments, FCF or DMSO was added during LLO exposure in M1 or M2

at 37°C for up to 30 min at 37ºC. TO-PRO-3 fluorescence intensity was measured in the temperature-controlled plate reader (Spectra Max i3X Multi-Mode Detection Platform, Molecular Devices) or by fluorescence microscopy as indicated in Figure Legends.

Fluorescence labeling. Cells were plated in a 24-well plate containing acid-washed glass slides. Cells were treated as indicated, washed twice in PHEM buffer (60 mM PIPES, 25 mM HEPES, 2 mM $MgCl_2$,10 mM EGTA; pH 6.9), fixed in 4% paraformaldehyde in PBS for 20 min at RT, and permeabilized for 5 min at RT with 0.1% Triton X-100 in PBS. Blocking was performed by incubating cells at RT for 1 h in PBS 10% serum and labeling by incubating cells with antibodies diluted in PBS, 10% serum for 30 min for all labeling except for the septins which were labeled for 2 h.

Microscopes, image acquisitions, and analyses. *Widefield microscopy (Nikon)*. Images were acquired using an automated, widefield Nikon Ti2-E microscope equipped with a blackout enclosure that is temperature, humidity, and CO_2-controlled; ten excitation wavelengths (Spectra III pad 365, 440, 488, 514, 561, 594, 640, and 730 nm) and emission filter sets for DAPI (435 ≤ emission ≤ 485 nm), CFP (460 ≤ emission ≤ 500 nm), FITC (515 ≤ emission ≤ 555 nm), YFP HYQ (from 520 ≤ emission ≤ 560 nm), Cy3 (from 573 ≤ emission ≤ 648 nm) and Texas Red HYQ (573 ≤ emission ≤ 648 nm) imaging with a high-speed wheel; back-thin illuminated SCMOS camera (Orca-Fusion BT, Hamamatsu) of resolution of 5.3 Megapixels; nanopositioning Piezo Sample Scanner (Prior). The automated stage allows multi-positioning (x-y) for high-content screening involving multi-well cell culture plates. The objectives include: 10x air Plan Apo lambda (0.45NA), 20x air S Plan Fluor ELWD (0.45 NA), 40x air S Plan Fluor ELWD 40x (0.6 NA), 40x water immersion (1.25NA), 40x air Plan Apo lambda (0.95 NA), a 60x water immersion Plan Apo IR (1.27NA). The imaging system has a “smart” auto-focus. NIS Elements AR Software was used for image analysis and NIS Elements HC Software for image acquisition. Images were randomly acquired from duplicate wells in each experimental condition. The number of independent experiments (N) is indicated in figure legends. For each field of view, 17 to 30 planes were acquired with a step size of 0.3 nm using a 60X water immersion objective. Image deconvolution was done using the Richardson-Lucy algorithm and the best-focused projection image was created using the extended depth of focus module. *Widefield microscopy (Zeiss).* Images were acquired on a motorized, inverted, wide-field fluorescence microscope (Axio Observer D1, TempModule S, heating unit XL S; Zeiss) equipped with a PZ-2000 XYZ automated stage, 20× Plan Neofluar (numerical aperture [NA] = 0.5), 40× Plan Neofluar (NA = 1.3), and 63× Plan

Apochromat (NA = 1.4) objectives, a high-speed Xenon fluorescence emission device (Lambda DG-4, 300 W; Sutter Instrument Company), a Lambda 10-3 optical emission filter wheel for the fluorescence imaging, a SmartShutter to control the illumination for phase-contrast and DIC imaging (Sutter Instrument Company), an ORCA-Flash 4.0 sCMOS camera (Hamamatsu). The filter sets for fluorescence was purchased from Chroma Technology Corporation and was as follows: DAPI (49000), Alexa Fluor 488 (49002), Alexa Fluor 568 (49005), and Cy5 (49006). Images were acquired and analyzed using MetaMorph imaging software (Molecular Devices). *SoRa confocal microscope (Nikon)*. Nikon Ti2-E microscope equipped with the Yokogawa CSU-W1 spinning disk with a 50 µm pinhole size (4000 rpm); a 60X Plan Apo lambda D OFN25 DIC N2 (NA 1.42) oil objective; and Quest Camera (apparent pixel size is 0.027 µm/pixel) from Hamamatsu. *Resonant laser scan confocal A1R plus (Nikon)*. Nikon Ti2-E microscope equipped with Plan Apo lambda 60x oil (NA 1.4), DU4 detector, pinhole size 39.59. For confocal images, 17-30 planes were acquired per field of view with a 0.2 nm step size. Images were denoised with denoise.ai (artificial intelligence) and deconvolved using the Richardson-Lucy algorithm (NIS Elements, Nikon).

Statistical analyses

For most of the data such as experiments with cell counts and fluorescence intensity as the measurements, log transformation was first used to reduce skewness and variation. ANOVA or linear mixed-effects models were then used for analyses depending on whether the data was independent or with repeated measurements over time. For the screening data, a p-value<0.05 without adjustment for multiple comparisons was used as the cutoff because the results were further validated in the subsequent assays. For all other tests, a p-value<0.05 for a single test or after adjustment for multiple comparisons with Holm's procedure was considered significant.

ABBREVIATIONS

Acid sphingomyelinase (ASM); ALG-2-interacting protein X (ALIX); Annexin A2 (ANXA2); Antibody (Ab); CDC (cholesterol-dependent cytolysins); Doxycycline (DOX); endosomal sorting complexes required for transport (ESCRT); ethylene glycol-bis(2-aminoethylether)-N,N,N',N',tetraacetic acid (EGTA); Forchlorfenuron (FCF); green-fluorescent histone 2B (H2B-GFP); Knobs (K); knockdown (KD); Listeriolysin O (LLO); Loops (L); MAC/PF (Membrane Attack Complex/Perforin); Number (N); Ratio (R); Room Temperature (RT); Septins (SEPT); short hairpin RNA (shRNA); silencing RNA (siRNA); Standard error of the mean (SEM); Supplemental Figure (SF); and Triton X-100 (TX-100)

ACKNOWLEDGMENTS

Research reported in this publication was supported by the Institute of Allergy and Infectious Diseases of the National Institutes of Health under award number R01AI157205. The content is solely the responsibility of the authors and does not necessarily represent the official views of the National Institutes of Health. Viviana Ruiz received financial public funding from the Colombian Ministry of Science, Technology, and Innovation (Ministerio de Ciencia, Tecnología e Innovación, MinCiencias). We acknowledge resources from the Campus Microscopy and Imaging Facility (CMIF) and the OSU Comprehensive Cancer Center (OSUCCC) Microscopy Shared Resource (MSR), The Ohio State University. This facility is supported in part by grant P30 CA016058, National Cancer Institute, Bethesda, MD. We also acknowledge the precious and kind help received from Dr. Anthony Vetter for assisting with fluorescence microscopy imaging and analysis using the NIS Elements software.

FIGURE LEGENDS

Figure 1. SEPT6 and SEPT7 expression is required for efficient plasma membrane repair. (**A**) HeLa cells were transfected with non-targeting siRNA (Ctrl siRNA) and with siRNAs targeting SEPT2, SEPT6, SEPT7, and SEPT9 (Supplemental Table 1). After 72 h, cells were lysed and analyzed by immunoblotting for septin and tubulin expression. Serial dilutions of control cell lysates (100% to 6.25%) and septin siRNA-treated cell lysates (100%) were loaded in the gel to facilitate the quantification of the KD efficiencies. Blots are representative of at least 5 independent experiments (N=5). KD efficiencies for SEPT6 were 39.5 $\pm$ 8.6; 3.6 $\pm$ 3.6; and 45.5 $\pm$ 12.5 for siRNA1, 2, and 3, respectively. KD efficiencies for all other septins were at least 90%. (**B to F**) HeLa cells were treated for 72 h with non-targeting or SEPT-specific siRNAs and were exposed to LLO (0.5 nM) for 30 min in M1 (1.2 mM Ca^{2+}) (B, D, E, F) or M2 (Ca^{2+}-free) (C) buffers, supplemented with TO-PRO-3. Data are the average TO-PRO-3 fluorescence intensities expressed in arbitrary units (AI) $\pm$ SEM of at least N=3 at time point 30 min. (**G**) Control HeLa cells and D_iSEPT7-shRNA HeLa cells were cultured for 72 h in the presence (+) or in the absence (-) of Dox (50 μg/ml) and were tested for SEPT7 KD efficiency by immunoblotting. The presented blot is representative of N=8 with a KD efficiency of 88.75$\pm$3.2% (Average $\pm$ SEM). (**H**) Control HeLa cells and D_iSEPT7-shRNA1 HeLa cells were cultured for 72 h in the presence or in the absence of DOX and then washed to remove the DOX. Cells were exposed, or not, to LLO for 30 min in M1 or M2 supplemented with TO-PRO-3. Data are expressed as the average ratio of the TO-PRO-3 fluorescence intensity of DOX-treated over TO-PRO-3 fluorescence intensity of non-treated (Ctr.) cells ($R_{Dox/Ctr.}$) $\pm$ SEM of N=5 at time point 30 min. (**I**) HeLa cells were pre-treated with 100 μM FCF (in DMSO), DMSO (1/500), or untreated (C) for 16 h. Cells were then subjected to the repair assay for 30 min with LLO in M1 or M2 buffers supplemented with TO-PRO-3. Due to FCF reversibility, FCF and DMSO were added to the buffers during the repair assay. Data are the average $\pm$ SEM of N=2 for Ca^{2+}- free condition and N=4 for 1.2 mM Ca^{2+} condition at 30 min time point. TO-PRO-3 intensity was measured by fluorescence microscopy (**B** and **G**) or by spectrofluorometry (**D**, **E**, **F**, and **I**). For **B-F** and **H-I** data were $\log_{10}$ transformed and analyzed using linear mixed effects models (*P< 0.05, **P< 0.01, *** P< 0.001, and **** P<0.0001).

Figure 2. The septin cytoskeleton is remodeled in LLO-perforated cells. HeLa cells were incubated without (Ctr.) or with LLO for 5-15 min at 37°C in repair permissive buffer M1 (1.2 mM Ca^{2+}). Cells were fixed, permeabilized and fluorescently labeled with anti-SEPT primary Abs and Alexa Fluor 568-conjugated secondary Ab, Alexa Fluor 488- or 647-conjugated phalloidin (F-

actin), and DAPI (nuclei). (**A, B**) Representative images at time point 15 min. Septin fluorescence images are presented with the same intensity scaling to visualize the loss of septin association with F-actin. To better visualize septin and actin filaments, selected regions were magnified (Ai-Aiii, Bi-Biii) and the septin fluorescence display was artificially enhanced in Aii and Bii. Scale bars are 10 μm and 2 μm (in Ai-Aiii, and Bi-Biii). All images were acquired by z-stack widefield microscopy, deconvolved, and presented as the best focus images, except for Aa and Ab images which are single planes focused on actin stress fibers. Knob and loop structures are indicated by unfilled and filled arrowheads, respectively.

Figure 3. Septin loop and knob formation increase over time in LLO-perforated cells. Cells were treated as indicated in Figure 2. (**A**) The percentage of cells with septin knobs and loops (%Cells with K+L) and (**B**) the average number of knobs or loops per total cell numbers ($N_{(K\ or\ L)}$/Total Cell) were enumerated. A total of 300-750 cells were analyzed in each experimental condition, N=3 independent experiments for the 15 min time point, and N=1 for the 5 and 10 min time points.

Figure 4. The septin cytoskeleton colocalizes with F-actin, myosin-IIA, and ANXA2 in LLO-perforated cells. HeLa cells were incubated with or without (Ctr.) LLO for 5-15 min at 37°C in repair permissive buffer M1 (1.2 mM Ca^{2+}). Cells were fixed, permeabilized and fluorescently labeled for microscopy analyses. (**A**) Representative images of cells labeled for SEPT2, F- Actin, and myosin-IIA at time point 15 min. Scale bars are 10 μm or 1 μm in zoomed regions. (**B, B'**) Representative images of non-transfected HeLa cells and HeLa cells transiently transfected to express ANX2-GFP, and labeled for ANXA2, SEPT2, F-actin, and nuclei at time point 15 min. Knob and loop structures are indicated by unfilled and filled arrowheads, respectively. Scale bar: 10 μm. (B') Enlarged regions from B to better visualize the septin colocalization with F-actin and ANXA2-GFP in both loop and non-loop regions. Fluorescence display was artificially enhanced in B'ii. Scale bar: 2 μm. (A, B, B') All images were acquired by z-stacks widefield microscopy, deconvolved, and presented as the best focus images. (**C**) The percentages of colocalization of the septins with ANXA2, F-actin, and ALIX were measured. A total of 300-750 cells were analyzed in each experimental condition, N=3 for the 15 min time point, except for ALIX colocalization and 5 and 10 min time points (N=1).

Figure 5. Redistribution of the septin cytoskeleton is functionally correlated with the plasma membrane repair efficiency. (**A**) HeLa cells were incubated with LLO for 15 min at 37°C

in M1 (1.2 mM Ca^{2+}) or M2 (Ca^{2+}-free) buffer. Cells were fixed, permeabilized, and fluorescently labeled for SEPT2, ANXA2, F-actin, and nuclei. Scale bars are 10 μm. (**B, C**) Control untreated HeLa cells (C) and HeLa cells pre-incubated with FCF (100 μM) or DMSO (1/500) for 16 h, were exposed to LLO in M1 or M2 (Ca^{2+}-free) buffer in the presence of FCF or DMSO, for 15 min at 37°C. The average number of septin knobs and loops per cell presenting such structures ($N_{(K+L)}$/Cell) (**B**), and the percentage of cells presenting these structures (% Cells with K+L) (**C**) were enumerated. A total of 300-750 cells were analyzed in each experimental condition from duplicate wells, N=3 at minimum. Linear mixed-effects models were used for analysis, **** P<0.0001. (**D**) HeLa cells were pre-incubated with 100 μM FCF, DMSO (1/500), or left untreated (Ctr.). Cells were then incubated with or without LLO (Ctr.) for 15 min at 37°C in M1 buffer. Equivalent concentrations of FCF and DMSO were maintained during LLO exposure. Cells were fixed, permeabilized, and fluorescently labeled for SEPT2, F-actin, and nuclei. Images were acquired by widefield microscopy (**A**) or resonant scanning confocal microscopy (**D**) and were denoised, deconvolved, and presented as best-focus projection images. Scale bars are 10 μm.

Figure 6. The septin cytoskeleton redistributes at the cell periphery in close association with the plasma membrane. (**A**) HeLa cells were transiently transfected to express the plasma membrane marker Lck-mTurquoise2 (Lck-mT2) and incubated with LLO for 15 min at 37°C in M1 buffer. Cells were fixed, permeabilized, and fluorescently labeled for SEPT2 and F-actin. Widefield Z-stack was deconvolved a single plane is presented. Scale bar is 10 μm. Arrows point to additional SEPT2, F-actin, and Lck colocalization. (Ai) and (Aii) are regions magnified from (A), scale bars are 1 μm. (**B, B'**) FCF-treated cells were exposed to LLO for 15 min at 37°C in M1 buffer and were fixed, permeabilized, and fluorescently labeled for SEPT2, ANXA2, and F-actin. Images were acquired by super-resolution spinning disk confocal microscopy. Image in (A) is a 3-D projection of all deconvolved images (44.99 μm x 56.07μm x 3.4 μm). A'i and A'ii show magnified regions from A to better visualize SEPT2, F-actin, and ANXA2. Scale bars are 1 μm. (**C**) The same image as in (B) but overlayed with a depth color code. (**D**) HeLa cells, pre-treated with 100 μM FCF, were treated with LLO for 15 min at 37°C in M1 buffer. Cells were fixed, permeabilized, and fluorescently labeled for SEPT2, F-actin, and nuclei. 3-D image of a denoised and deconvolved Z-stack acquired by resonant scanning confocal microscopy (106 μm x 106 μm x 5 μm). (**Di**) 3-D magnified projection of (D) (6 μm x 8 μm x 5 μm). All images (A-D) were labeled with anti-SEPT2 primary Ab and Alexa Fluor 568-conjugated secondary Ab, Alexa Fluor 647-

conjugated phalloidin (F-Actin), nuclei (DAPI), and (A, A', B, and Di) anti-ANXA2 primary Ab and Alexa Fluor 488-conjugated secondary Ab.

Figure 7. F-actin and ANXA2 redistributions is dependent on SEPT7 expression. (A) HeLa cells were transfected with a non-targeting siRNA (Ctrl. siRNA) or with SEPT7-siRNA 1 and incubated with LLO, or not (Ctr.), for 15 min at 37°C in M1 buffer. Cells were fixed, permeabilized, and SEPT2 (Alexa Fluor 568-conjugated secondary Ab), F-Actin (Alexa Fluor 647-conjugated phalloidin), ANXA2 (Alexa Fluor 488-conjugated secondary Ab), and nuclei (DAPI) were labeled. The presented images are the best-focus projections from deconvolved Z-stacks acquired by widefield microscopy and are displayed with the same intensity scaling for each fluorescence setting. Scale bars are 10 μm. (**Ai**) and (**Aii**) are regions magnified from (A), scale bars are 2 μm. (**B**) The number of septin knobs and loops per total cells (N_{K+L}/ Total cells) were enumerated in cells labeled with anti-SEPT2, -SEPT7, or -SEPT9 antibodies. A total of 150-300 cells were analyzed from duplicate wells, per experimental condition. N=1, error bars are ± SEM values of the internal replicates.

Supplemental Figure 1 (**A** to **D**) HeLa cells were transfected with a non-targeting siRNA (Ctrl. siRNA) and with siRNAs targeting the septins. Three non-overlapping silencing sequences were used for each septin (Supplemental Table 1). After 72 h, cells were lysed and analyzed by immunoblotting for septin and tubulin expression. Blots are representative of at least N=5 independent experiments. (**C**) Comparing control siRNA-treated cells to SEPT7-siRNA-treated cells, SEPT6 expression was reduced by 44.8% ± 24.4; 70% ± 21.2; and 52.3% ± 19.6 for siRNA1, 2, and 3, respectively, SEPT2 expression was reduced by 59.6% ± 4.3; 46.4% ± 7.7; and 40.1% ± 6.9 for siRNA1, 2, and 3, respectively. SEPT 9 expression was reduced by at least 90% for all three siRNAs. KD of SEPT2, 6, and 9 did not appear to significantly affect the expression of the other tested septins. (**E**) Two stable HeLa cell lines, D_iSEPT7-shRNA1 and D_iSEPT7-shRNA2, were generated by transduction of lentiviral vectors encoding inducible SEPT7 shRNA followed by their selection on puromycin as detailed in materials and methods. The two cell lines were cultured for 48 and 72 h with DOX (50 μg/ml) or for 72 h in the absence of DOX (-). Cell lysates were analyzed by immunoblotting and the KD efficiencies, expressed as a percentage expression relative to control cells cultured in the absence of DOX are indicated in the figure. (**F**) The hemolytic assay showed that the presence of Dox at the indicated concentrations does not affect LLO pore formation. Note that in the repair assay, DOX-treated cells were washed three times, so only traces of DOX were present in the medium during the repair assay. (**G**, **H**) HeLa cells

were pre-treated with the indicated concentrations of FCF, or corresponding DMSO dilutions, or left untreated (Ctr.) for 16 h. Equivalent concentrations of FCF and DMSO were maintained in the buffer during the repair assay. Cells were exposed to LLO for 30 min in M1 or M2 buffer supplemented with TO-PRO-3. Kinetic data are expressed as the average TO-PRO-3 fluorescence intensities in arbitrary unit of N=2 to 4 independent experiments (each with 4 to 8 technical replicates) ± SEM at each time point. (**I**) The hemolytic assay showed that FCF at the highest concentration does not affect LLO pore formation.

Supplemental Figure 2. HeLa cells were incubated without (Ctr.) or with LLO for 5-15 min at 37°C in M1 buffer. Cells were chemically fixed, permeabilized, and fluorescently labeled with anti-SEPT9, or SEPT7, or SEPT2 primary Abs (Alexa Fluor 568-conjugated secondary Ab), Alexa Fluor 488-conjugated phalloidin (F-Actin), and nuclei (DAPI). (**A**) SEPT9 fluorescence images are presented with the same intensity scaling to show the loss of septin association with F-actin. To better visualize septin and actin filaments, selected regions were magnified (Ai- Aiii) and the septin fluorescence display was artificially enhanced in Aii. Septin knobs and loops are indicated by unfilled and filled arrowheads, respectively. Scale bars are 10 μm and 2 μm in Ai- Aiii. (**B**) The numbers of septin knobs or loops per cell which present such structures ($N_{(K\ or\ L)}$/Cells) were enumerated at the indicated time points. A total of 300-750 cells were analyzed in each experimental condition from duplicate wells, N=3 for the 15 min time point, and N=1 for 5 and 10 min time points. (**C**) Cells were fluorescently labeled for SEPT2, F-Actin, ALIX, and nuclei at time point 15 min. Scale bars: 10 μm. (**D**) HeLa cells were transfected with the non-targeting siRNA (Ctrl. siRNA) and with SEPT7-siRNA 1. Cells were incubated without LLO for 15 min at 37°C in M1 buffer. Cells were fixed, permeabilized and labeled with anti-SEPT primary Ab (Alexa Fluor 568-conjugated secondary Ab), Alexa Fluor 488-conjugated phalloidin (F-Actin), and DAPI (nuclei). Scale bars: 10 μm. (A, C, D) Z-stack images were acquired by widefield microscopy, deconvolved, and displayed as best-focus projection images except for (C) which are single plane images.

Supplemental Table 1: List of genes and corresponding silencing sequences used in this work. Gene identification (Gene ID) provides the link to the National Library of Medicine gene references. siRNA ID are the reference from the ThermoFisher catalogue.

Supplemental Table 2: Total cell numbers were enumerated pre- and post-kinetic in each well of the 96 well plates based on fluorescence microscopy imaging of H2BGFP-expressing HeLa

cells as we previously described (Lam et al., 2019). Cell numbers are the average of four wells in each experimental condition and presented data are post-kinetic. Experimental samples are the average counts of cells targeted with specific siRNAs. Controls 1 to 3 are the counts of control cells plated at 100% (Control 1), 90% (Control 2), and 80% (Control 3) and treated with irrelevant siRNA. In yellow are experimental conditions which were not considered in our assay due to ratio of experimental sample to control outside of a 15% range.

Supplemental Table 3: siRNA screen to identify genes controlling plasma membrane repair. The screen was conducted with HeLa H2B-GFP cells and targeted 245 genes with a cocktail of 3 non-overlapping siRNAs. The assay measured TO-PRO-3 fluorescence intensity as a read out for plasma membrane integrity of cells incubated in the presence or absence of LLO. Data are the statistical analyses comparing cells treated with specific KD to cell treated with irrelevant siRNA. Italicized are genes with a negative effect on plasma membrane integrity. In bold are genes already known to control plasma membrane repair.

Supplemental Table 4: Sequences used in this work. The silencing sequences are highlighted in grey.

* SEPTIN 7 shRNA sequence obtained from the Genetic Perturbation Platform (Broad Institute).
** SEPTIN 7 shRNA sequences previously tested (Sellin et al., 2011)

Literature Cited

Abbey, M., C. Hakim, R. Anand, J. Lafera, A. Schambach, A. Kispert, M.H. Taft, V. Kaever, A. Kotlyarov, M. Gaestel, and M.B. Menon. 2016. GTPase domain driven dimerization of SEPT7 is dispensable for the critical role of septins in fibroblast cytokinesis. *Sci Rep*. 6:20007.

Andrade, L.O. 2019. Plasma membrane repair involvement in parasitic and other pathogen infections. *Curr Top Membr*. 84:217-238.

Ayyar, B.V., K. Ettayebi, W. Salmen, U.C. Karandikar, F.H. Neill, V.R. Tenge, S.E. Crawford, E. Bieberich, B.V.V. Prasad, R.L. Atmar, and M.K. Estes. 2023. CLIC and membrane wound repair pathways enable pandemic norovirus entry and infection. *Nat Commun*. 14:1148.

Banerji, R., A. Karkee, P. Kanojiya, and S.D. Saroj. 2021. Pore-forming toxins of foodborne pathogens. *Compr Rev Food Sci Food Saf*. 20:2265-2285.

Barisch, C., J.C.M. Holthuis, and K. Cosentino. 2023. Membrane damage and repair: a thin line between life and death. *Biol Chem*.

Bement, W.M., C.A. Mandato, and M.N. Kirsch. 1999. Wound-induced assembly and closure of an actomyosin purse string in Xenopus oocytes. *Curr Biol*. 9:579-587.

Benaud, C., G. Le Dez, S. Mironov, F. Galli, D. Reboutier, and C. Prigent. 2015. Annexin A2 is required for the early steps of cytokinesis. *EMBO Rep*. 16:481-489.

Benoit, B., C. Pous, and A. Baillet. 2023. Septins as membrane influencers: direct play or in association with other cytoskeleton partners. *Front Cell Dev Biol*. 11:1112319.

Bi, G.Q., J.M. Alderton, and R.A. Steinhardt. 1995. Calcium-regulated exocytosis is required for cell membrane resealing. *J Cell Biol*. 131:1747-1758.

Bouillot, S., E. Reboud, and P. Huber. 2018. Functional Consequences of Calcium Influx Promoted by Bacterial Pore-Forming Toxins. *Toxins (Basel)*. 10.

Cassidy, S.K., J.A. Hagar, T.D. Kanneganti, L. Franchi, G. Nunez, and M.X. O'Riordan. 2012. Membrane damage during Listeria monocytogenes infection triggers a caspase-7 dependent cytoprotective response. *PLoS Pathog*. 8:e1002628.

Chen, C., B.N. Nguyen, G. Mitchell, S.R. Margolis, D. Ma, and D.A. Portnoy. 2018. The Listeriolysin O PEST-like Sequence Co-opts AP-2-Mediated Endocytosis to Prevent Plasma Membrane Damage during Listeria Infection. *Cell Host Microbe*. 23:786-795 e785.

Czuczman, M.A., R. Fattouh, J.M. van Rijn, V. Canadien, S. Osborne, A.M. Muise, V.K. Kuchroo, D.E. Higgins, and J.H. Brumell. 2014. Listeria monocytogenes exploits efferocytosis to promote cell-to-cell spread. *Nature*. 509:230-234.

DeMay, B.S., R.A. Meseroll, P. Occhipinti, and A.S. Gladfelter. 2010. Cellular requirements for the small molecule forchlorfenuron to stabilize the septin cytoskeleton. *Cytoskeleton (Hoboken)*. 67:383-399.

Dias, C., and J. Nylandsted. 2021. Plasma membrane integrity in health and disease: significance and therapeutic potential. *Cell Discov*. 7:4.

Dunstone, M.A., and R.K. Tweten. 2012. Packing a punch: the mechanism of pore formation by cholesterol dependent cytolysins and membrane attack complex/perforin-like proteins. *Curr Opin Struct Biol*. 22:342-349.

Escrevente, C., L. Bento-Lopes, J.S. Ramalho, and D.C. Barral. 2021. Rab11 is required for lysosome exocytosis through the interaction with Rab3a, Sec15 and GRAB. *J Cell Sci*. 134.

Frank, S.B., V.V. Schulz, and C.K. Miranti. 2017. A streamlined method for the design and cloning of shRNAs into an optimized Dox-inducible lentiviral vector. *BMC Biotechnol*. 17:24.

Goldfine, H., C. Knob, D. Alford, and J. Bentz. 1995. Membrane permeabilization by Listeria monocytogenes phosphatidylinositol-specific phospholipase C is independent of phospholipid hydrolysis and cooperative with listeriolysin O. *Proc Natl Acad Sci U S A*. 92:2979-2983.

Goldfine, H., S.J. Wadsworth, and N.C. Johnston. 2000. Activation of host phospholipases C and D in macrophages after infection with Listeria monocytogenes. *Infect Immun*. 68:5735-5741.

Hu, Q., W.J. Nelson, and E.T. Spiliotis. 2008. Forchlorfenuron alters mammalian septin assembly, organization, and dynamics. *J Biol Chem*. 283:29563-29571.

Idone, V., C. Tam, J.W. Goss, D. Toomre, M. Pypaert, and N.W. Andrews. 2008. Repair of injured plasma membrane by rapid Ca2+-dependent endocytosis. *J Cell Biol*. 180:905-914.

Iwase, M., S. Okada, T. Oguchi, and A. Toh-e. 2004. Forchlorfenuron, a phenylurea cytokinin, disturbs septin organization in Saccharomyces cerevisiae. *Genes Genet Syst*. 79:199-206.

Jaiswal, J.K., S.P. Lauritzen, L. Scheffer, M. Sakaguchi, J. Bunkenborg, S.M. Simon, T. Kallunki, M. Jaattela, and J. Nylandsted. 2014. S100A11 is required for efficient plasma membrane repair and survival of invasive cancer cells. *Nat Commun*. 5:3795.

Jimenez, A.J., P. Maiuri, J. Lafaurie-Janvore, S. Divoux, M. Piel, and F. Perez. 2014. ESCRT machinery is required for plasma membrane repair. *Science*. 343:1247136.

Kinoshita, M. 2003. Assembly of mammalian septins. *J Biochem*. 134:491-496.

Koerdt, S.N., A.P.K. Ashraf, and V. Gerke. 2019. Annexins and plasma membrane repair. *Curr Top Membr*. 84:43-65.

Kremer, B.E., T. Haystead, and I.G. Macara. 2005. Mammalian septins regulate microtubule stability through interaction with the microtubule-binding protein MAP4. *Mol Biol Cell*. 16:4648-4659.

Lam, J.G.T., C. Song, and S. Seveau. 2019. High-throughput Measurement of Plasma Membrane Resealing Efficiency in Mammalian Cells. *J Vis Exp*.

Lam, J.G.T., S. Vadia, S. Pathak-Sharma, E. McLaughlin, X. Zhang, J. Swanson, and S. Seveau. 2018. Host cell perforation by listeriolysin O (LLO) activates a Ca(2+)-dependent cPKC/Rac1/Arp2/3 signaling pathway that promotes Listeria monocytogenes internalization independently of membrane resealing. *Mol Biol Cell*. 29:270-284.

Mavrakis, M., Y. Azou-Gros, F.C. Tsai, J. Alvarado, A. Bertin, F. Iv, A. Kress, S. Brasselet, G.H. Koenderink, and T. Lecuit. 2014. Septins promote F-actin ring formation by crosslinking actin filaments into curved bundles. *Nat Cell Biol*. 16:322-334.

McNeil, P.L. 2002. Repairing a torn cell surface: make way, lysosomes to the rescue. *J Cell Sci*. 115:873-879.

Mellgren, R.L., W. Zhang, K. Miyake, and P.L. McNeil. 2007. Calpain is required for the rapid, calcium-dependent repair of wounded plasma membrane. *J Biol Chem*. 282:2567-2575.

Nakamura, M., J. Hui, and S.M. Parkhurst. 2023. Bending actin filaments: twists of fate. *Fac Rev*. 12:7.

Nozaki, K., V.I. Maltez, M. Rayamajhi, A.L. Tubbs, J.E. Mitchell, C.A. Lacey, C.K. Harvest, L. Li, W.T. Nash, H.N. Larson, B.D. McGlaughon, N.J. Moorman, M.G. Brown, J.K. Whitmire, and E.A. Miao. 2022. Caspase-7 activates ASM to repair gasdermin and perforin pores. *Nature*. 606:960-967.

Osborne, S.E., and J.H. Brumell. 2017. Listeriolysin O: from bazooka to Swiss army knife. *Philos Trans R Soc Lond B Biol Sci*. 372.

Petrisic, N., M. Kozorog, S. Aden, M. Podobnik, and G. Anderluh. 2021. The molecular mechanisms of listeriolysin O-induced lipid membrane damage. *Biochim Biophys Acta Biomembr*. 1863:183604.
Rall, J.A. 2019. Calcium and muscle contraction: the triumph and tragedy of Lewis Victor Heilbrunn. *Adv Physiol Educ*. 43:476-485.
Ray, S., R. Roth, and P.A. Keyel. 2022. Membrane repair triggered by cholesterol-dependent cytolysins is activated by mixed lineage kinases and MEK. *Sci Adv*. 8:eabl6367.
Rescher, U., N. Zobiack, and V. Gerke. 2000. Intact Ca(2+)-binding sites are required for targeting of annexin 1 to endosomal membranes in living HeLa cells. *J Cell Sci*. 113 (Pt 22):3931-3938.
Robertin, S., and S. Mostowy. 2020. The history of septin biology and bacterial infection. *Cell Microbiol*. 22:e13173.
Rogers, S., R. Wells, and M. Rechsteiner. 1986. Amino acid sequences common to rapidly degraded proteins: the PEST hypothesis. *Science*. 234:364-368.
Russo, G., and M. Krauss. 2021. Septin Remodeling During Mammalian Cytokinesis. *Front Cell Dev Biol*. 9:768309.
Satoh, H., Y. Nakano, H. Shibata, and M. Maki. 2002. The penta-EF-hand domain of ALG-2 interacts with amino-terminal domains of both annexin VII and annexin XI in a Ca2+-dependent manner. *Biochim Biophys Acta*. 1600:61-67.
Schuerch, D.W., E.M. Wilson-Kubalek, and R.K. Tweten. 2005. Molecular basis of listeriolysin O pH dependence. *Proc Natl Acad Sci U S A*. 102:12537-12542.
Sellin, M.E., L. Sandblad, S. Stenmark, and M. Gullberg. 2011. Deciphering the rules governing assembly order of mammalian septin complexes. *Mol Biol Cell*. 22:3152-3164.
Seveau, S. 2014. Multifaceted activity of listeriolysin O, the cholesterol-dependent cytolysin of Listeria monocytogenes. *Subcell Biochem*. 80:161-195.
Sonder, S.L., T.L. Boye, R. Tolle, J. Dengjel, K. Maeda, M. Jaattela, A.C. Simonsen, J.K. Jaiswal, and J. Nylandsted. 2019. Annexin A7 is required for ESCRT III-mediated plasma membrane repair. *Sci Rep*. 9:6726.
Spiliotis, E.T., and K. Nakos. 2021. Cellular functions of actin- and microtubule-associated septins. *Curr Biol*. 31:R651-R666.
Tam, C., V. Idone, C. Devlin, M.C. Fernandes, A. Flannery, X. He, E. Schuchman, I. Tabas, and N.W. Andrews. 2010. Exocytosis of acid sphingomyelinase by wounded cells promotes endocytosis and plasma membrane repair. *J Cell Biol*. 189:1027-1038.
Thapa, R., S. Ray, and P.A. Keyel. 2020. Interaction of Macrophages and Cholesterol-Dependent Cytolysins: The Impact on Immune Response and Cellular Survival. *Toxins (Basel)*. 12.
Togo, T., T.B. Krasieva, and R.A. Steinhardt. 2000. A decrease in membrane tension precedes successful cell-membrane repair. *Mol Biol Cell*. 11:4339-4346.
Vadia, S., E. Arnett, A.C. Haghighat, E.M. Wilson-Kubalek, R.K. Tweten, and S. Seveau. 2011. The pore-forming toxin listeriolysin O mediates a novel entry pathway of L. monocytogenes into human hepatocytes. *PLoS Pathog*. 7:e1002356.
Vadia, S., and S. Seveau. 2014. Fluxes of Ca2+ and K+ are required for the listeriolysin O-dependent internalization pathway of Listeria monocytogenes. *Infect Immun*. 82:1084-1091.
Zacharias, D.A., J.D. Violin, A.C. Newton, and R.Y. Tsien. 2002. Partitioning of lipid-modified monomeric GFPs into membrane microdomains of live cells. *Science*. 296:913-916.

Figure 1

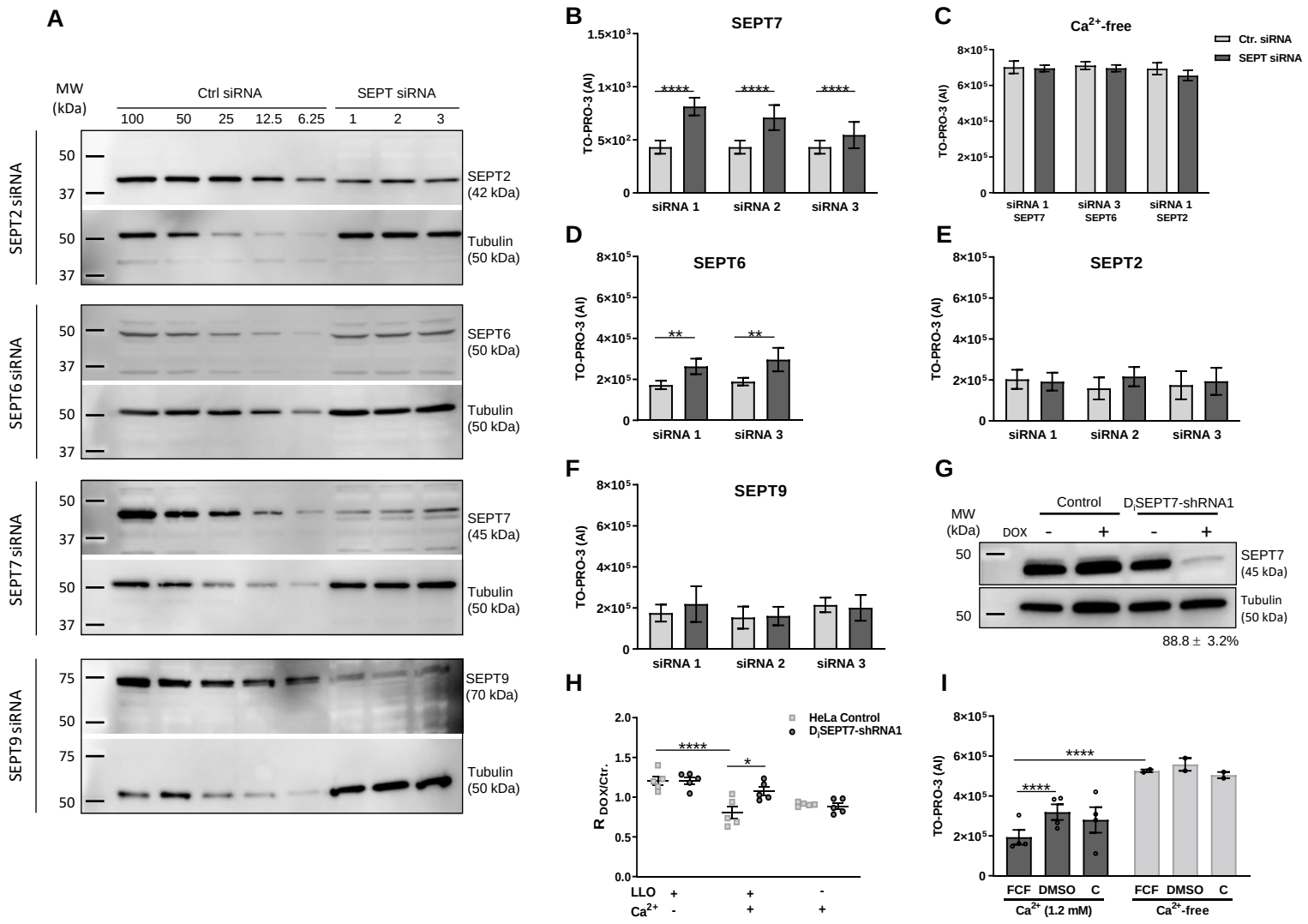
A
MW (kDa)
Ctrl siRNA
SEPT siRNA
100 50 25 12.5 6.25 1 2 3
SEPT2 siRNA
SEPT2 (42 kDa)
Tubulin (50 kDa)
SEPT6 siRNA
SEPT6 (50 kDa)
SEPT7 siRNA
SEPT7 (45 kDa)
SEPT9 siRNA
SEPT9 (70 kDa)
B
SEPT7
TO-PRO-3 (AI)
siRNA 1
siRNA 2
siRNA 3
C
Ca2+-free
Ctr. siRNA
SEPT siRNA
siRNA 1 SEPT7
siRNA 3 SEPT6
siRNA 1 SEPT2
D
SEPT6
E
SEPT2
F
SEPT9
G
Control
DiSEPT7-shRNA1
DOX
SEPT7 (45 kDa)
Tubulin (50 kDa)
88.8 ± 3.2%
H
HeLa Control
DiSEPT7-shRNA1
R DOX/Ctr.
LLO
Ca2+
I
FCF DMSO C
Ca2+ (1.2 mM)
Ca2+-free

Figure 2

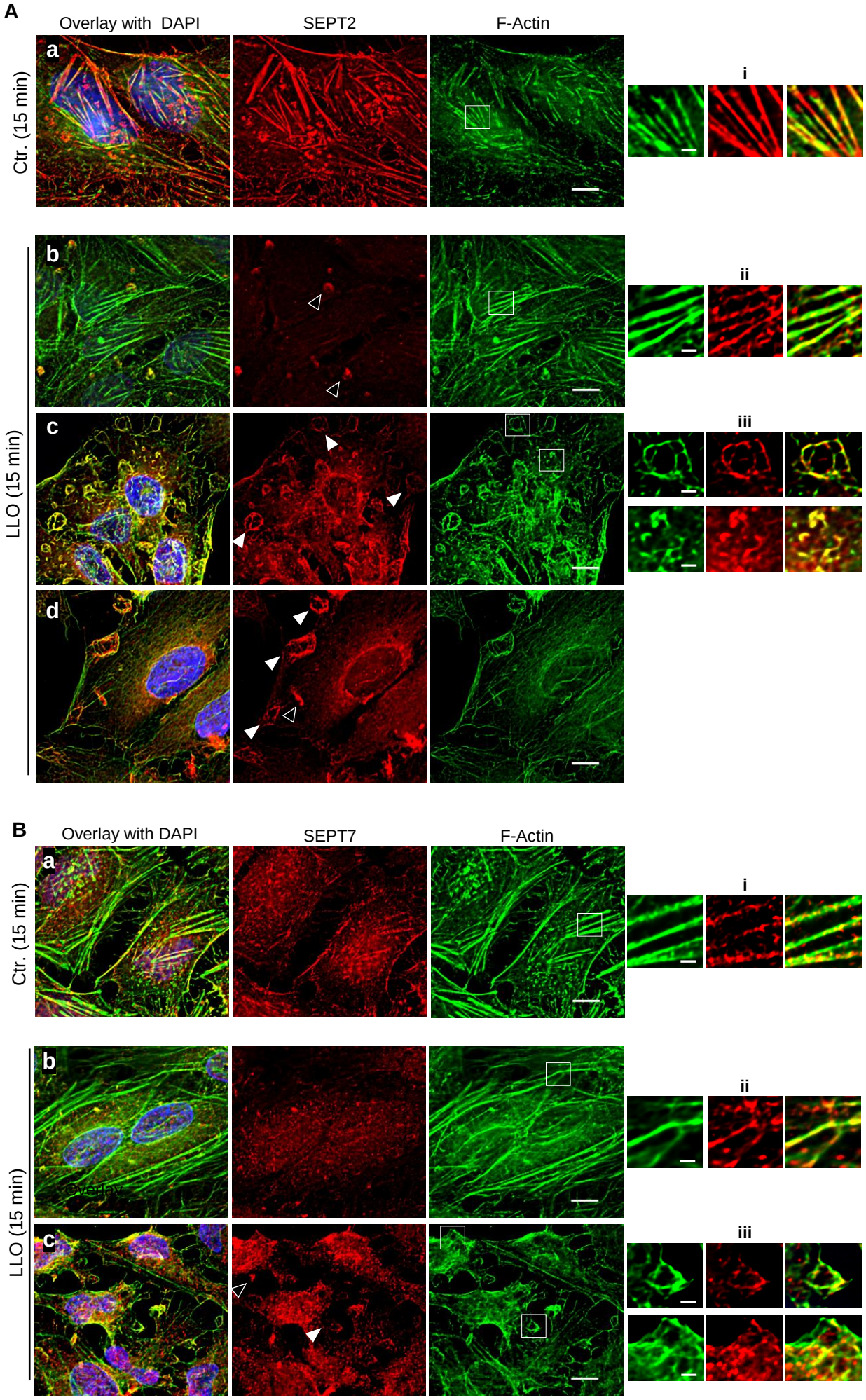
A
Overlay with DAPI
SEPT2
F-Actin
Ctr. (15 min)
LLO (15 min)
a
b
c
d
i
ii
iii
B
Overlay with DAPI
SEPT7
F-Actin
Ctr. (15 min)
LLO (15 min)
a
b
c
Overlay
i
ii
iii

Figure 3

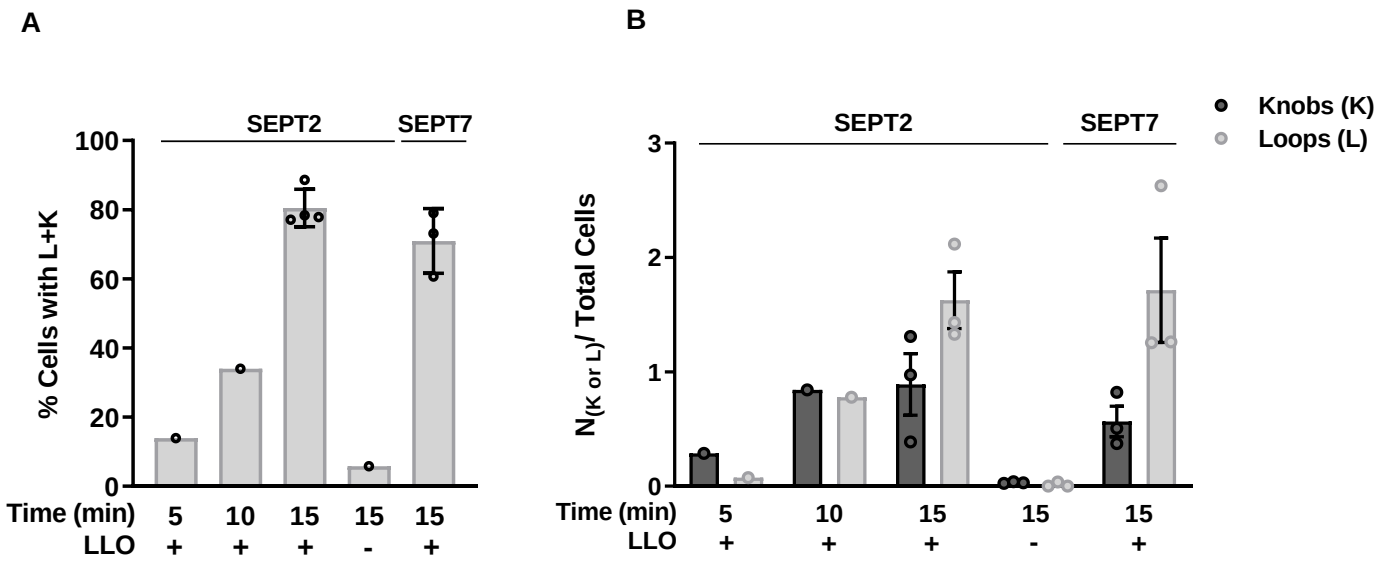
A
SEPT2
SEPT7
% Cells with L+K
100
80
60
40
20
0
Time (min) 5 10 15 15 15
LLO + + + - +
B
SEPT2
SEPT7
Knobs (K)
Loops (L)
N(K or L)/ Total Cells
3
2
1
0
Time (min) 5 10 15 15 15
LLO + + + - +

Figure 4

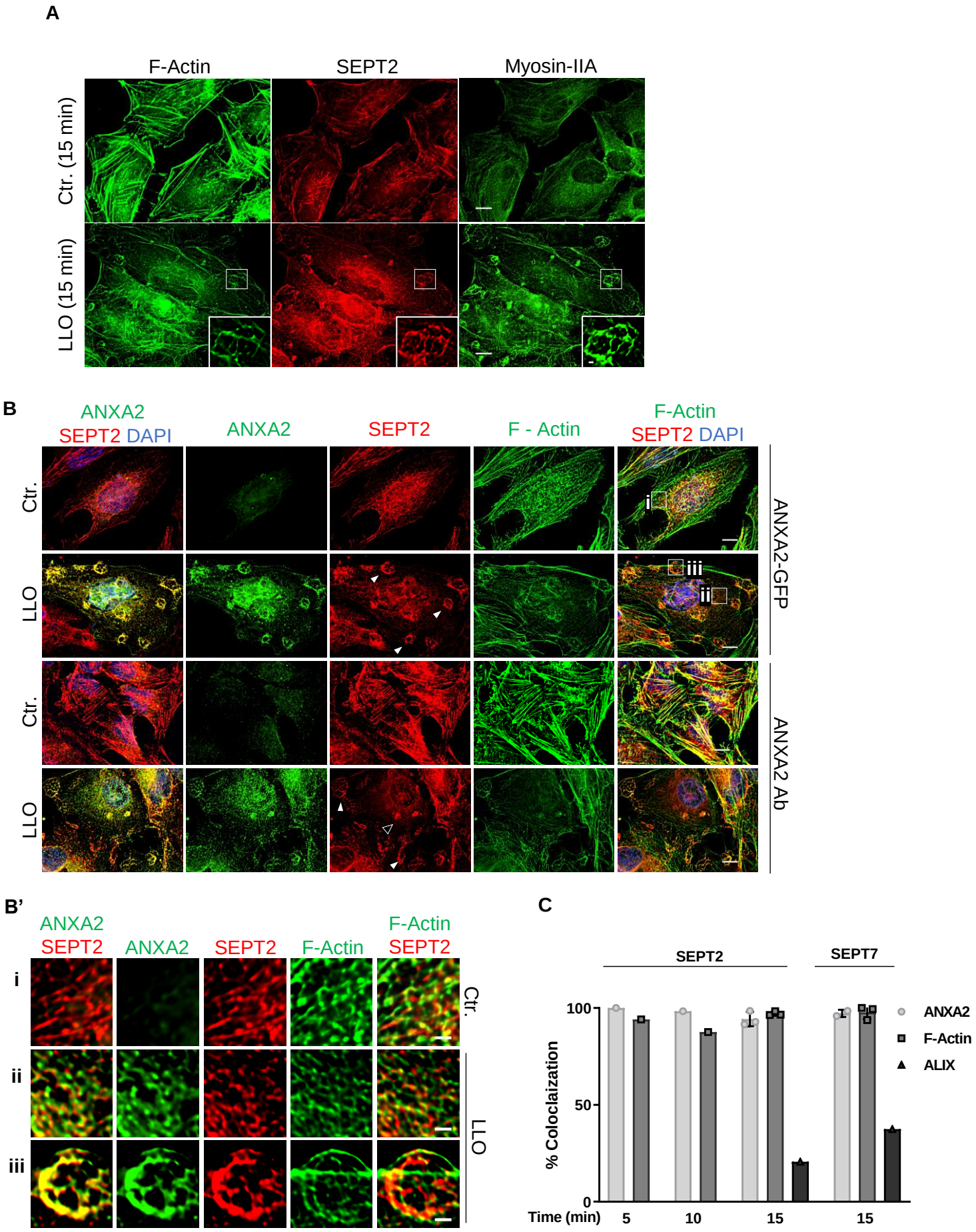
A
F-Actin
SEPT2
Myosin-IIA
Ctr. (15 min)
LLO (15 min)
B
ANXA2
SEPT2 DAPI
ANXA2
SEPT2
F - Actin
F-Actin
SEPT2 DAPI
Ctr.
LLO
Ctr.
LLO
i
ii
iii
ANXA2-GFP
ANXA2 Ab
B'
ANXA2
SEPT2
ANXA2
SEPT2
F-Actin
F-Actin
SEPT2
i
ii
iii
Ctr.
LLO
C
SEPT2
SEPT7
% Coloclaization
100
50
0
Time (min)
5
10
15
15
ANXA2
F-Actin
ALIX

Figure 5

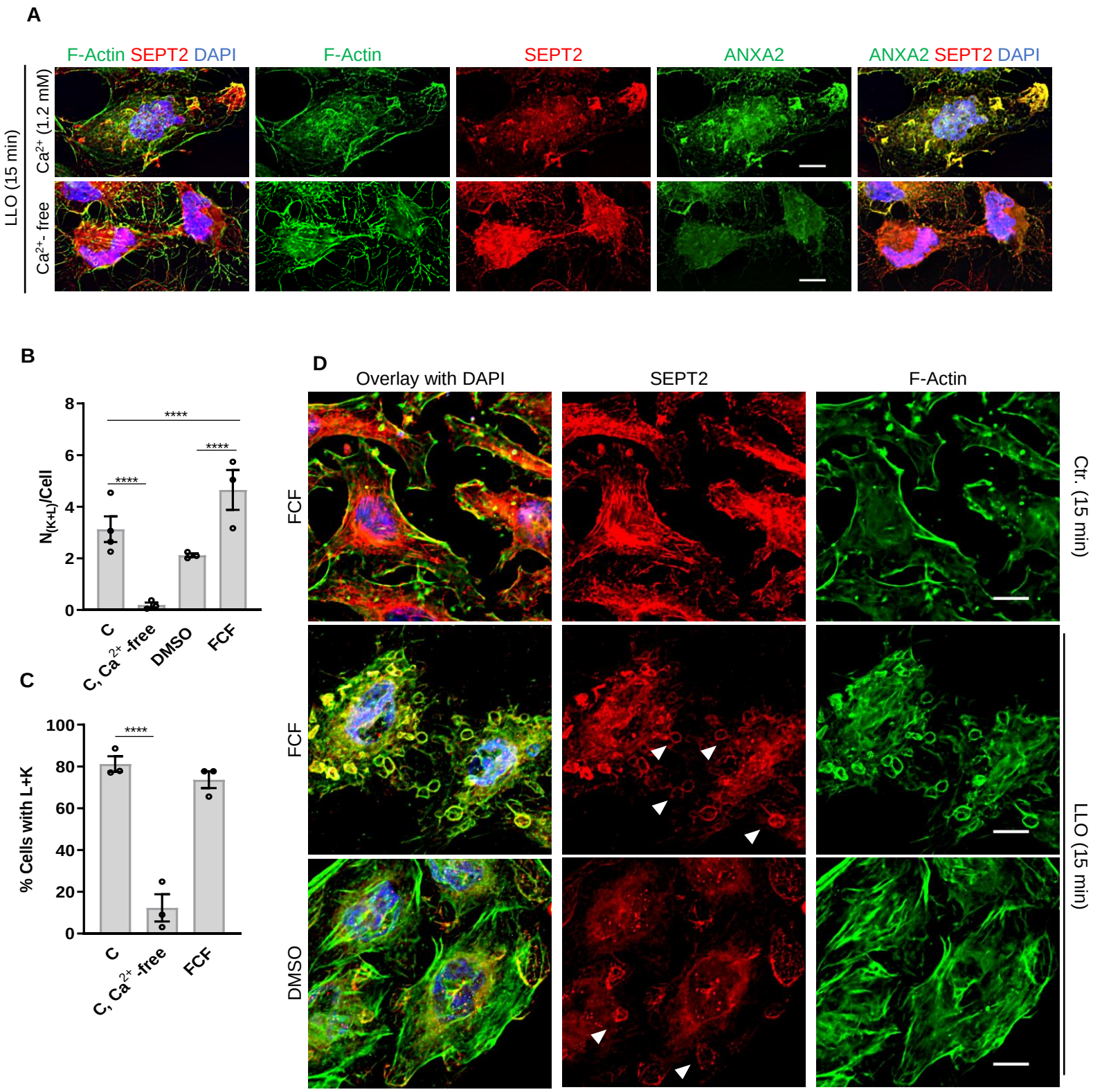
A
F-Actin SEPT2 DAPI
F-Actin
SEPT2
ANXA2
ANXA2 SEPT2 DAPI
LLO (15 min)
Ca2+ (1.2 mM)
Ca2+- free
B
N(K+L)/Cell
****
C
C, Ca2+ -free
DMSO
FCF
C
% Cells with L+K
D
Overlay with DAPI
SEPT2
F-Actin
Ctr. (15 min)
LLO (15 min)

Figure 6

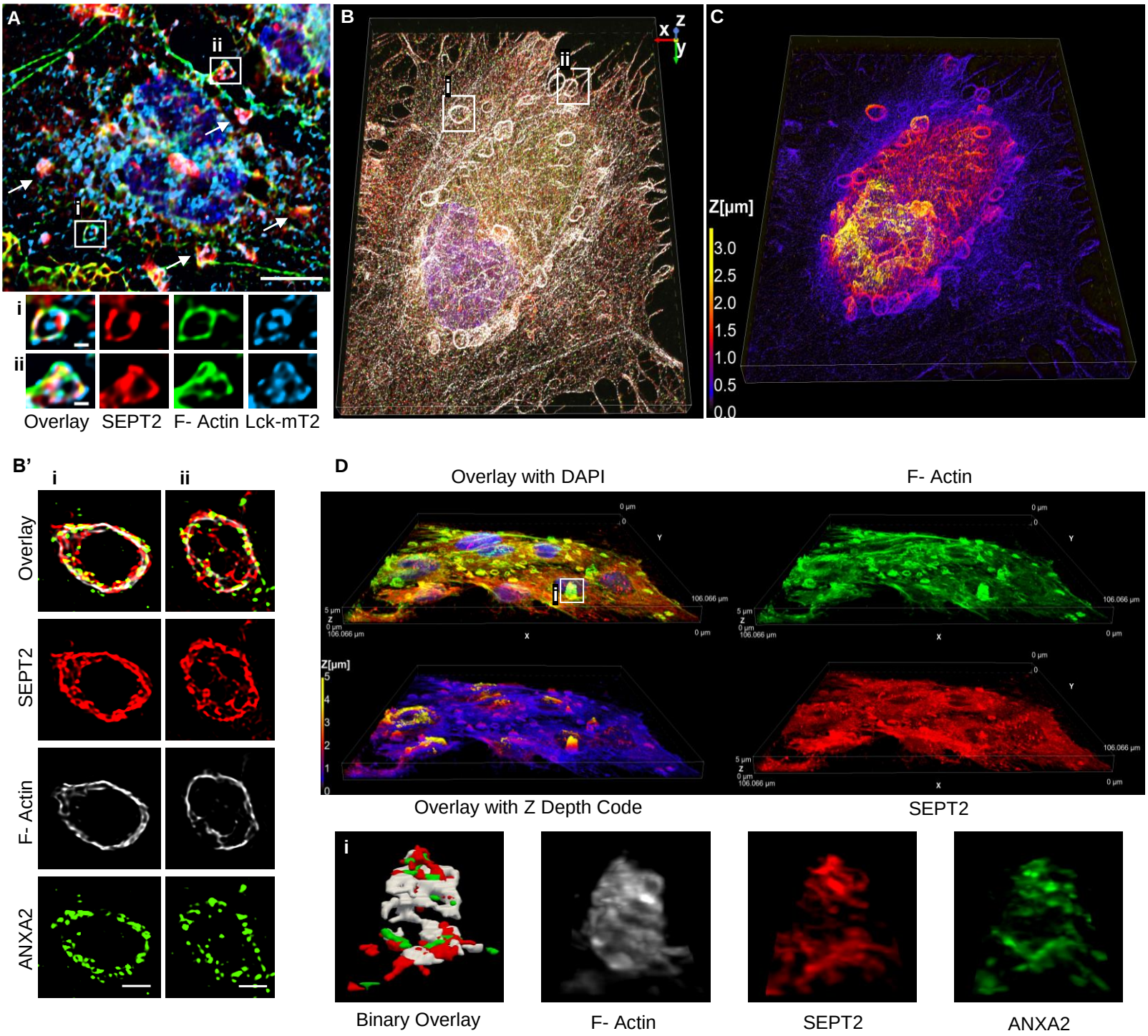
A
ii
i
i
ii
Overlay
SEPT2
F- Actin
Lck-mT2
B
x
z
y
ii
i
C
Z[µm]
3.0
2.5
2.0
1.5
1.0
0.5
0.0
B'
i
ii
Overlay
SEPT2
F- Actin
ANXA2
D
Overlay with DAPI
F- Actin
i
Z[µm]
Overlay with Z Depth Code
SEPT2
i
Binary Overlay
F- Actin
SEPT2
ANXA2

Figure 7

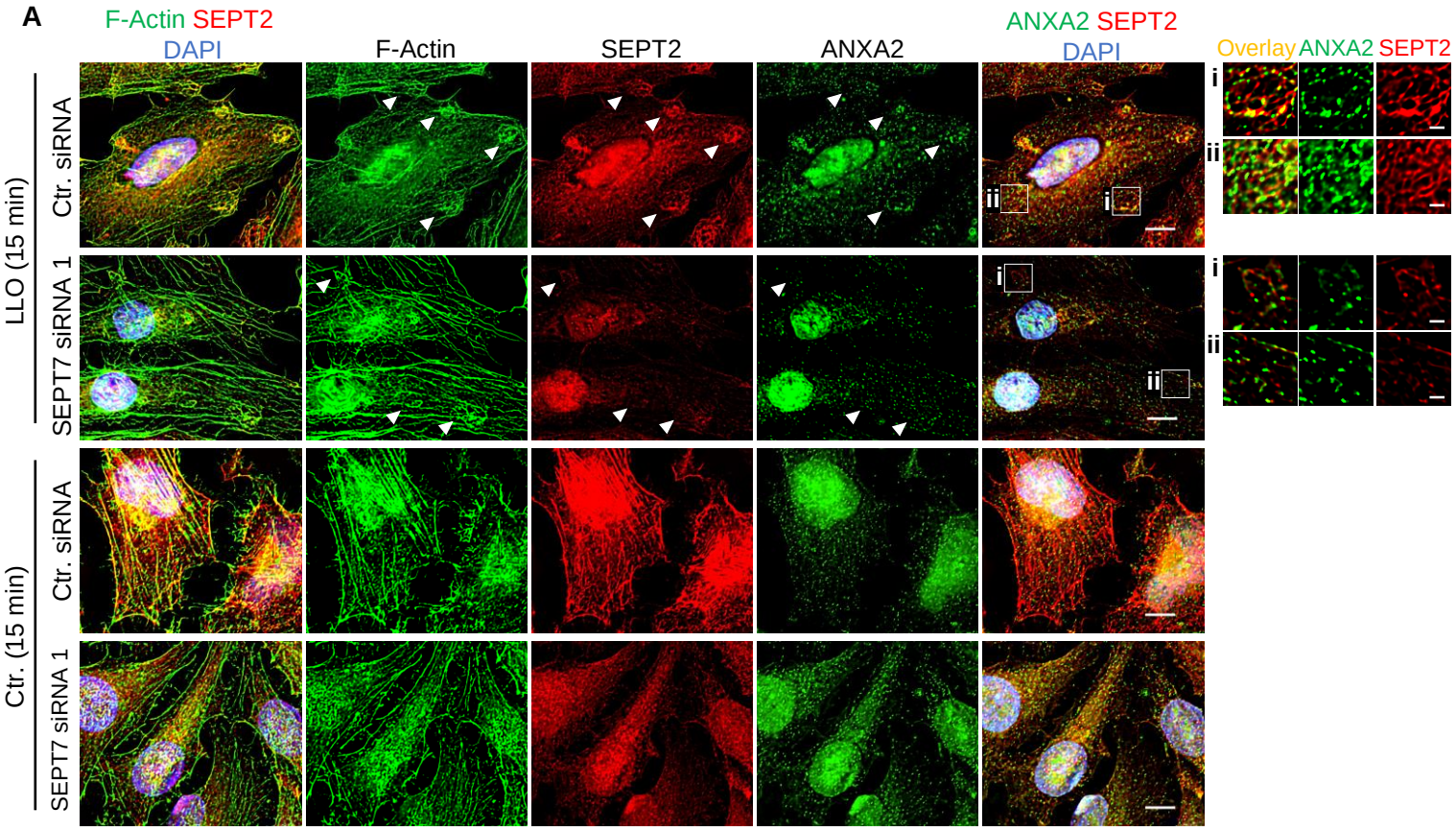
A
F-Actin SEPT2
DAPI
F-Actin
SEPT2
ANXA2
ANXA2 SEPT2
DAPI
Overlay ANXA2 SEPT2
LLO (15 min)
Ctr. siRNA
SEPT7 siRNA 1
Ctr. (15 min)
Ctr. siRNA
SEPT7 siRNA 1
i
ii

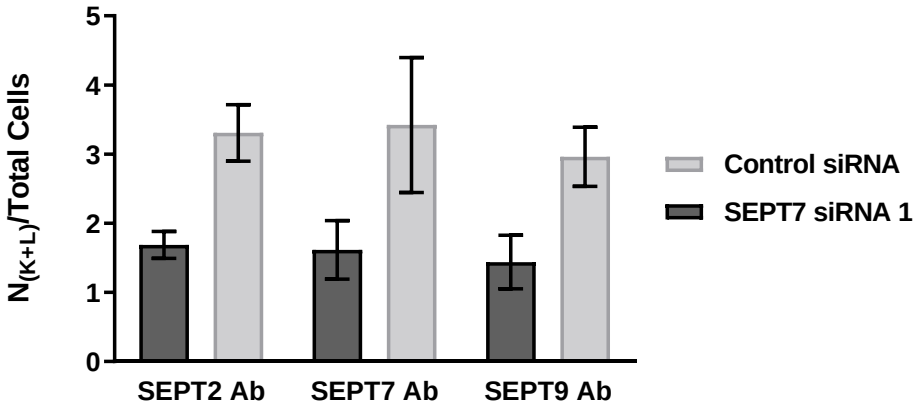
B
N(K+L)/Total Cells
0
1
2
3
4
5
SEPT2 Ab
SEPT7 Ab
SEPT9 Ab
Control siRNA
SEPT7 siRNA 1